RMetS
Royal Meteorological Society

Inner-core vacillation cycles during the intensification of Hurricane *Katrina*

Mai C. Nguyen,[a]* Michael J. Reeder,[a] Noel E. Davidson,[b] Roger K. Smith[c] and Michael T. Montgomery[d]

[a] *School of Mathematical Sciences, Monash University, Melbourne, Australia*
[b] *Centre for Australian Weather and Climate Research, Bureau of Meteorology, Melbourne, Australia*
[c] *Meteorological Institute, University of Munich, Munich, Germany*
[d] *Department of Meteorology, Naval Postgraduate School, Monterey, CA, USA*
*Correspondence to: M. C. Nguyen, School of Mathematical Sciences, Monash University, Melbourne, Australia.
E-mail: Mai.Nguyen@sci.monash.edu.au

A simulation of Hurricane *Katrina* (2005) using the Australian Bureau of Meteorology's operational model for tropical-cyclone prediction (TCLAPS) shows that the simulated vortex vacillates between almost symmetric and highly asymmetric phases. During the symmetric phase, the eyewall comprises elongated convective bands and both the low-level potential vorticity (PV) and pseudo-equivalent potential temperature θ_e fields exhibit a ring structure, with the maximum at some radius from the vortex centre. During this phase the mean flow intensifies comparatively rapidly, as the maximum acceleration of the mean tangential wind occurs near the radius of maximum mean tangential wind (RMW). In contrast, during the asymmetric phase the eyewall is more polygonal, with vortical hot towers (VHTs) located at the vertices. The low-level PV and θ_e fields have monopole structures with the maximum at the centre. The intensification rate is lower than during the symmetric phase because the mean tangential wind accelerates most rapidly well within the RMW.

The symmetric-to-asymmetric transition is accompanied by the development of VHTs within the eyewall. The VHTs are shown to be initiated by barotropic–convective instability associated with the ring-like structure of PV in the eyewall where the convective instability is large. During the reverse asymmetric-to-symmetric transition, the VHTs weaken as the local vertical wind shear increases and the convective available potential energy is consumed by convection. The weakened VHTs move outwards, similar to vortex Rossby waves, and are stretched by the angular shear of the mean vortex. Simultaneously, the rapid filamentation zone outside the RMW weakens, becoming more favourable for the development of convection. The next symmetric phase emerges as the convection reorganizes into a more symmetric eyewall. It is proposed that vacillation cycles occur in young tropical cyclones and are distinct from the eyewall replacement cycles that tend to occur in strong and mature tropical cyclones. Copyright © 2011 Royal Meteorological Society

Key Words: tropical cyclone; vortex Rossby waves; barotropic instability; vortical hot towers; eyewall replacement cycles; rapid filamentation zones; vacillation cycles

Received 29 October 2010; Revised 23 February 2011; Accepted 7 March 2011; Published online in Wiley Online Library 17 May 2011

Citation: Nguyen MC, Reeder MJ, Davidson NE, Smith RK, Montgomery MT. 2011. Inner-core vacillation cycles during the intensification of Hurricane *Katrina*. *Q. J. R. Meteorol. Soc.* **137**: 829–844. DOI:10.1002/qj.823

1. Introduction

The changes in intensity of tropical cyclones and the associated changes in their inner-core structure have been studied for nearly half a century. The key result from the early work is that a tropical cyclone intensifies as the symmetric overturning circulation draws air from outer radii above the boundary layer while conserving absolute angular momentum. This symmetric intensification mechanism was first successfully simulated by Ooyama (1969). The

contraction of the symmetric eyewall was explained later by Shapiro and Willoughby (1982) in the theoretical framework devised by Eliassen (1951). The approach was to solve for the response of a symmetric balanced vortex to imposed local sources of heat and momentum representing the eyewall. Based on aircraft data, Willoughby (1990) showed that tropical-cyclone intensification is normally accompanied by contraction of the maximum of the axisymmetric swirling wind. More recently, the symmetric spin-up problem has been revisited by Smith *et al.* (2009), who have shown that the inner core intensifies by the radial convergence of absolute angular momentum within the boundary layer, despite some frictional loss, whereas convergence above the boundary layer strengthens the winds at outer radii.

Tropical-cyclone intensification by internal processes has received considerable attention over the last two decades. Several important processes and phenomena have been discovered, including those in which asymmetries play important roles. The inner-core processes most relevant to the intensification of the vortex are

(1) eyewall replacement cycles (ERCs) (Willoughby *et al.*, 1982),
(2) vortex Rossby waves (VRWs) (Guinn and Schubert, 1993; Montgomery and Kallenbach, 1997; Möller and Montgomery, 1999, 2000),
(3) barotropic instability and eyewall mesovortices (Schubert *et al.*, 1999; Kossin and Schubert, 2001) and
(4) vortical hot towers (VHTs) (Hendricks *et al.*, 2004; Montgomery *et al.*, 2006; Tory *et al.*, 2006; Nguyen *et al.*, 2008).

Although they occur in the same small area of the inner core of a tropical cyclone, these processes have mostly been studied separately and in different contexts. As a first step to understanding inner-core intensity and structure changes, it is pertinent to explore the relationship between these processes and tropical-cyclone intensification in a model.

The present study examines how these different mechanisms change the intensity of tropical cyclones. For this purpose, a high-resolution (0.05° horizontal resolution) version of the Australian Bureau of Meteorology's operational model for tropical-cyclone prediction (TCLAPS) is used to simulate Hurricane *Katrina* (2005). TCLAPS is a hydrostatic, limited-area numerical weather prediction model, which includes a tropical-cyclone bogus scheme and assimilation technique specially designed for predicting tropical cyclones. Details of this model and the vortex initialization procedure therein are described by Davidson and Puri (1992), Puri *et al.* (1998) and Davidson and Weber (2000).

An ensemble of simulations of Hurricane *Katrina* has been performed using different initial and boundary conditions, different configurations of the model and different initial vortex structures, the details of which can be found in Nguyen (2010). The simulated track and intensity of most of the members show good agreement with the observations from Hurricane *Katrina*. Moreover, during the intensification stage*, most of the ensemble members exhibit vacillations between almost symmetric and highly asymmetric states in association with marked changes in the rates of intensification. The vortex structures during these two phases are similar to the two regimes found in the flight-level data collected over a 20 year period (1977–1996) for Atlantic hurricanes and reported by Kossin and Eastin (2001). In the first regime, which often accompanies rapid intensification, the profiles of vorticity and equivalent potential temperature (θ_e) exhibit a ring structure with elevated values near the eyewall and smaller values in the eye. In contrast, in the second regime, a monopole structure with maximum at the centre is observed for both vorticity and θ_e. The present work focuses on the evolution of these changes in the vortex structure.

This article presents a detailed analysis of the vortex structure during the two phases for a particular member of the ensemble. The ensemble member chosen is the one that most closely matches the observations. It uses the boundary conditions from analyses of the Australian Global ASimmilation Prediction model (GASP) and sea-surface temperature analysis of the same week (which was normally unavailable in real time). The physical mechanisms involved in the transitions between the two phases are identified and related to the inner-core processes described above.

This article is organized as follows. Section 2 describes the evolution of the simulated Hurricane *Katrina*, paying particular attention to the development of asymmetries in the PV. In section 3, the structure of the simulated hurricane during the two phases is analyzed and compared with satellite images of Hurricane *Katrina*. The physical processes that occur during transitions between the two phases are discussed in section 4 and our conclusions are presented in section 5.

2. The evolution of the hurricane and development of asymmetries

The flow asymmetries are characterized here by the amplitudes of different azimuthal wave numbers at 850 hPa, obtained by Fourier decomposition, and the maximum standard deviation of potential vorticity (PV) from its azimuthal mean, SDPVmax.

Figure 1 shows the evolution of the PV asymmetries at 850 hPa, with SDPVmax shown in panel (a) and the amplitudes of azimuthal wave numbers 0–6 at 50 km radius in panel (b). In this simulation, which starts at 0000 UTC on 26 August 2005, there are three phases during which the vortex is prominently asymmetric: these phases are denoted by A1, A2 and A3 and run from 28–32 h, 42–46 h and 52–57 h, respectively. The maximum amplitudes of the PV asymmetries occur at times t_{A1} = 31 h, t_{A2} = 44 h and t_{A3} = 54 h (see Figure 1(a)). Increases in the amplitude of the asymmetries during these phases are associated with the amplification of wave numbers 2–4 (Figure 2(b)). These asymmetric phases are separated by two prominent phases of relatively high symmetry (i.e. with a minimum in SDPVmax) between 37–40 h and 49–50 h. We refer to these as symmetric phases S1 and S2, respectively. The maximum symmetry occurs at times t_{S1} = 39 h and t_{S2} = 50 h, respectively. During the symmetric phases, the amplitude of the symmetric component, wave number 0, is relatively large, while those of the asymmetric components, wave numbers greater than 0, are small (Figure 1(b)). Thus, the symmetric component is largest during the symmetric phase, but decreases rapidly in amplitude as the asymmetric structures grow.

*The intensification stages are classified in a similar way to that used in Zhu *et al.* (2001) and Nguyen *et al.* (2002), comprising the gestation stage, the intensification stage and the mature stage. The intensification stage begins when deep convective structures are initiated in the inner core region.

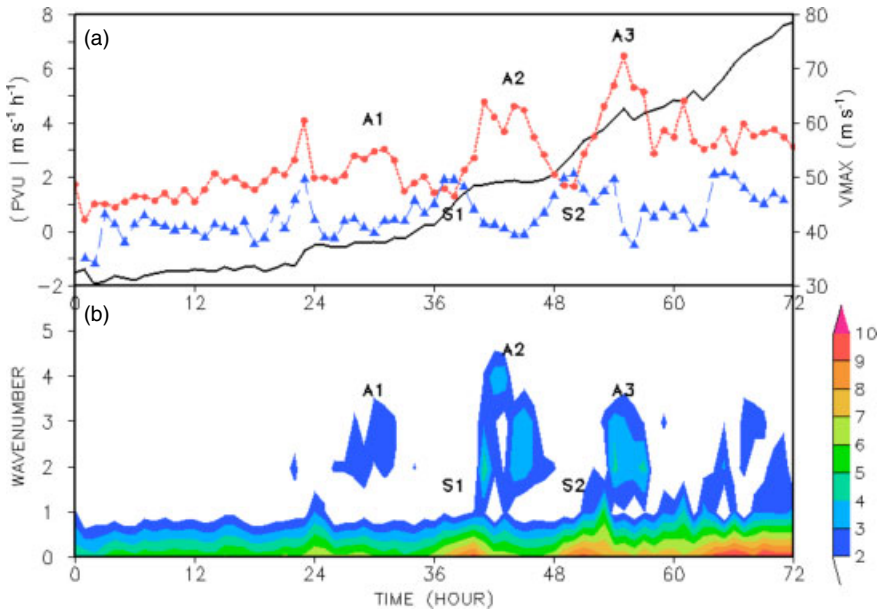

Figure 1. Evolution of PV asymmetries at 850 hPa: (a) SDPVmax (dotted line with circles, red in online article [PV Unit = $10^6 \times$ m^{-2} K kg^{-1}]), maximum mean tangential wind $\bar{v}_{max}$ (solid black line [m s^{-1}]) and its tendency $\partial\bar{v}_{max}/\partial t$ (dashed line with triangles, blue in online article [m s^{-1} h^{-1}]). (b) Amplitudes of azimuthal wave numbers from 0–6 of PV [PVU] at 50 km radius. The horizontal axis shows hours elapsed from 0000 UTC on 26 August 2005. This figure is available in colour online at wileyonlinelibrary.com/journal/qj

It has been shown by several authors (Black *et al.*, 2002; Rogers *et al.*, 2003; Braun *et al.*, 2006) that wave number 1 asymmetries tend to be associated with environmental vertical wind shear. In the present simulation, the model-derived deep-layer shear (i.e. the difference between the mean winds at 200 hPa and 850 hPa levels) is relatively small, less than 5 m s^{-1} during the period S1–A3 (Nguyen, 2010). Accordingly, throughout the integration period the amplitude of wave number 1 is indeed small (Figure 1(b)). Thus the evolution of asymmetries in the model is unlikely to be associated with environmental vertical wind shear and seems more likely to be connected to internal processes in the inner core.

The variation of the asymmetries is highly correlated with the rate of change of the maximum azimuthal-mean tangential wind $\partial\bar{v}_{max}/\partial t$. (Note especially the anticorrelation between the dashed line with circles and the solid line with triangles in Figure 1(a).) The correlation coefficient between SDPVmax and $\partial\bar{v}_{max}/\partial t$ is relatively high (-0.7) during the period from 31 h (t_{A1}) to 54 h (t_{A3}) and even higher over shorter time periods (e.g. -0.92 from 39–54 h). This correlation is consistent with the observational study of Willoughby (1990), which showed that more symmetric tropical cyclones tend to have higher intensification rates than those that are more asymmetric.

Figure 2 shows the evolution of the maximum azimuthal mean tangential wind $\bar{v}_{max}$ at 850 hPa, maximum total wind speed at any level[†] and minimum surface pressure. The minimum surface pressure falls most rapidly during the asymmetric phases, the reasons for which will be discussed in section 4.1. In contrast, both maximum azimuthal mean and total wind increase rapidly during the symmetric phases, but change little during the asymmetric phases. The maximum total wind speed peaks during the asymmetric phases before decreasing ahead of the next symmetric phase. The occurrence of strong winds during the asymmetric phase

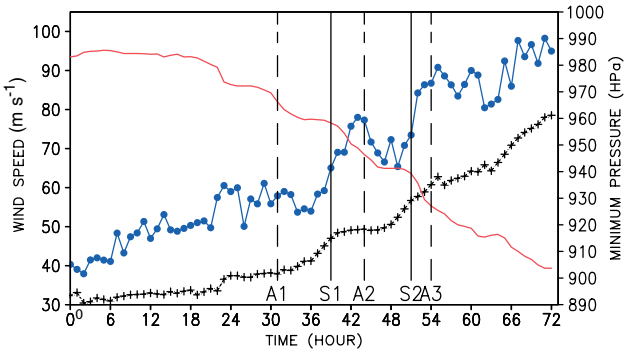

Figure 2. Evolution of maximum mean tangential wind at 850 hPa (dotted black line with crosses), maximum total wind (solid line with circles, blue in online article) and minimum surface pressure (solid line, red in online article). This figure is available in colour online at wileyonlinelibrary.com/journal/qj

is associated with VHTs, which develop within the eyewall (shown in the next section), and is a result of the increased vertical vorticity produced by the vorticity stretching in the updraught of the VHTs. In this article, VHT refers to a convective updraught with a nearly coincident cyclonic potential vorticity anomaly in the low to mid troposphere. The operation of the physical mechanisms described herein does not require these updraughts to penetrate all the way to the tropopause (Wissmeier and Smith, 2011).

In summary, the simulated tropical cyclone vacillates between states of relatively high and low symmetry while intensifying. These vacillation cycles are the focus of the remainder of this study.

3. The evolution of the vortex

3.1. *Symmetric and asymmetric phases*

The structure of the vortex at 850 hPa at times t_{S1} and t_{A2} is examined now (Figure 3). The vertical velocity

[†]The maximum typically occurs near 900 hPa.

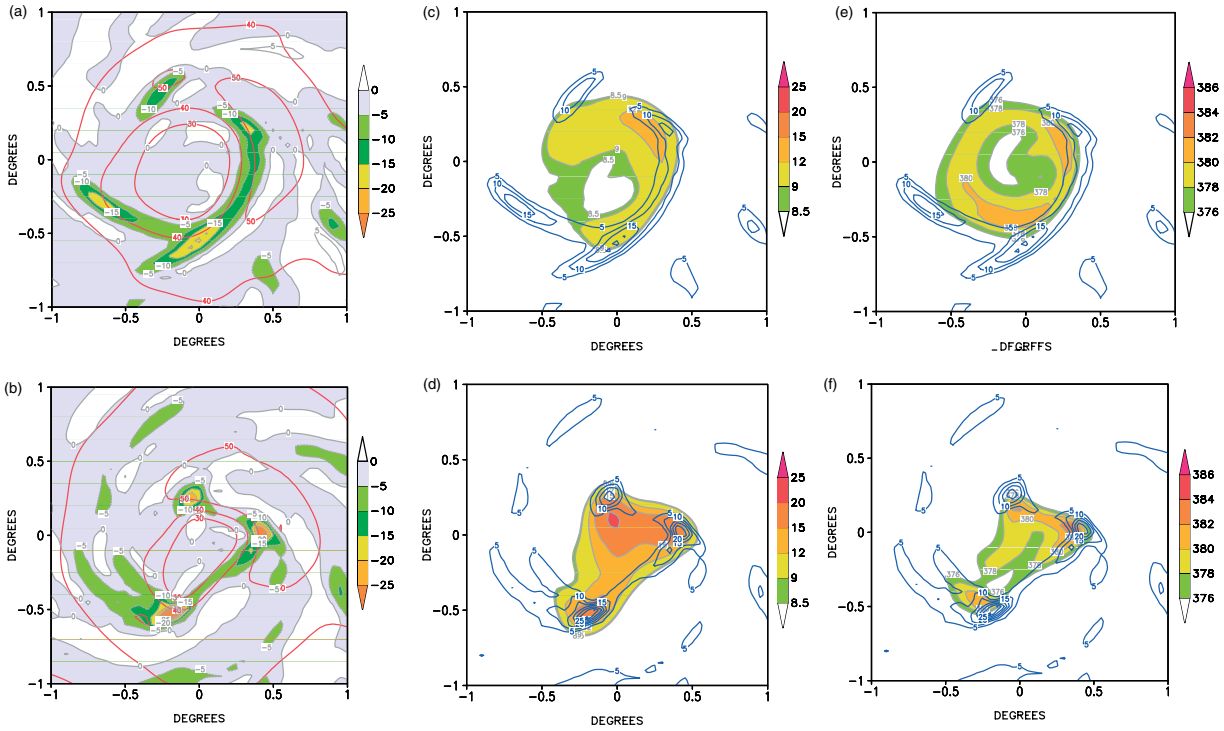

Figure 3. Vortex structure at 850 hPa during symmetric phase S1 (top panels) and asymmetric phase A2 (bottom panels). (a) and (b) Vertical velocity in pressure coordinates [Pa s^{-1}] (updraughts are shaded) and horizontal wind magnitude (contours). (c) and (d) PV [PVU] (shaded). (e) and (f) Equivalent potential temperature θ_e [K] (shaded). The contours in panels (c)–(f) are vertical velocity. This figure is available in colour online at wileyonlinelibrary.com/journal/qj

fields at these two times (Figure 3(a) and (b)) show distinctly different features. Although there are still noticeable asymmetries, the eyewall[‡] at t_{S1} has a quasi-ring-like structure comprising elongated bands of moderately strong updraught. In contrast, at t_{A2} the eyewall has a triangular shape with three intense updraughts at the vertices. These updraughts have enhanced rotation and are the model representation of VHTs.

The structure of the PV at times t_{S1} and t_{A2} is shown in Figure 3(c) and (d) respectively, and the corresponding θ_e structures are shown in Figure 3(e) and (f). At time t_{S1}, both fields have a ring-like structure with maxima at radii of about 35 km, while at t_{A2} they have a monopole structure with maxima located near the centre.

The foregoing structures are representative of phases S1 and A2, respectively, and are also similar during the other phases of strong symmetry (S2) and asymmetry (A1). For this reason, subsequently we use the times t_{S1} and t_{A2} to illustrate the characteristics of the symmetric and asymmetric phases, respectively.

During the symmetric and asymmetric phases, the vortex structure in the simulation is similar to the observed structure during Regimes 1 and 2 reported by Kossin and Eastin (2001), which is described in section 1. There are other aspects of the simulation that are also similar to Kossin and Eastin's regimes. First, the rate of intensification is higher during their Regime 1 than during Regime 2. Second, the transition from Regime 1 to 2 occurs over a short time interval (typically 1–2 h). The time-scale for the reverse transition is not reported by Kossin and Eastin (2001), whereas it is about 4–6 h in the simulation.

The simulation allows one to investigate a range of fields not readily available from observations such as local wind speed, surface heat fluxes and rate of strain. These fields are of interest because of their relevance to understanding the role of VHTs during the asymmetric phase and are shown in Figure 4 at times t_{S1} and t_{A2}. The regions of locally high wind speed at 850 hPa in Figure 4(a) and (b) are highlighted by the negative Laplacian of the wind speed ($-\nabla^2 V_{\mathrm{mag}}$). Figure 4(c) and (d) show the surface latent heat flux and Figure 4(e) and (f) show the horizontal rate of strain at 850 hPa. The horizontal rate of strain, S, is defined by $S^2 = (\partial U/\partial x - \partial V/\partial y)^2 + (\partial V/\partial x + \partial U/\partial y)^2$, where U and V are wind components in the zonal and meridional directions x and y, respectively.

During the asymmetric phase, the VHTs are clearly associated with strong local wind speeds (Figure 4(b)), high θ_e values (Figure 3(f)) at 850 hPa and enhanced surface fluxes (Figure 4(d)). The collocation of these dynamical and thermodynamical features may be understood as follows. Bursts of convection increase the surface wind speed in their vicinity as air is drawn into an updraught. In turn, the increased wind speeds enhance the surface latent heat fluxes, increasing θ_e at low levels. As a result, the buoyancy of the air within the updraughts of the VHTs is enhanced, leading to stronger convection. In contrast, during the symmetric phase (Figures 4(a), 3(e) and 4(c)) these variables have comparatively lower magnitudes and more axisymmetric structures, consistent with the ring-like eyewall.

There is a region of large rate of strain just outside the eyewall during both the symmetric and asymmetric phases (Figure 4(e) and (f), respectively). This region is associated in part with the strong radial shear of the azimuthal mean tangential flow and in part with the strong horizontal shear associated with VHTs during the asymmetric phase. In this

[‡]The eyewall is defined arbitrarily as the regions having an the minimum upward velocity of −5 Pa s^{-1}, which is equivalent to 50 cm s^{-1} at 850 hPa.

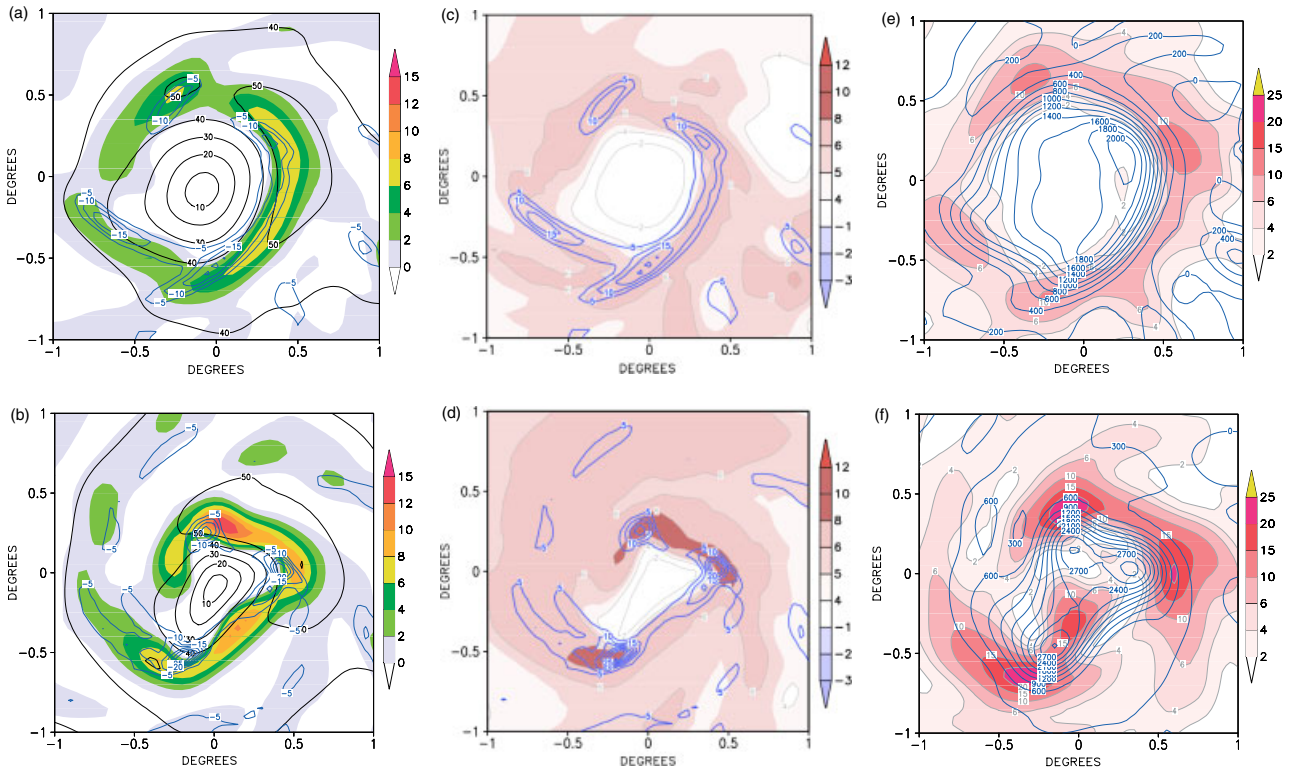

Figure 4. As Figure 3 but for other fields. (a) and (b) Laplacian of the horizontal wind magnitude $-\nabla^2 V_{\mathrm{mag}}$ $[10^{-8}\times (\mathrm{m\,s})^{-1}]$ (shaded); grey (black in the online colour version) contours show horizontal wind speed. (c) and (d) Surface latent heat flux (shaded, $[10^2\times \mathrm{W\,m^{-2}}]$. Dark (blue) contours in panels (a)–(d) show vertical velocity. (e) and (f) Horizontal rate of strain S^2 (shaded, $[10^{-7}\times \mathrm{s^{-2}}]$). Contours show relative vorticity $[10^3\times \mathrm{s^{-1}}]$. This figure is available in colour online at wileyonlinelibrary.com/journal/qj

area, there is a large negative radial gradient of relative vorticity compared with the weak gradient in the core region, where the relative vorticity is comparatively large. For this reason, the flow changes from one with relatively large vorticity and low rate of strain in the core to one with low vorticity and large rate of strain outside the core. Rozoff *et al.* (2006) proposed that rapid filamentation zones, where the square of rate of strain (S^2) is larger than the enstrophy (ζ^2), are unfavourable for convection if the filamentation time-scale ($\tau_{\mathrm{fil}} = (S^2 - \zeta^2)^{-1/2}$) is less than the convective time-scale. Thus, during the asymmetric phase (Figure 4(f)), the large rate of strain and hence strong filamentation occurring just outside the VHTs are unfavourable for the development of convection.

Another significant difference between the symmetric and asymmetric phases is the area of large rate of strain inside the eyewall during the asymmetric phase (Figure 4(f)). This region has comparatively high values of vorticity (see contours), which are associated with VHTs. Consequently the vorticity is rapidly stirred in the region between the eye and the eyewall during the asymmetric phase.

3.2. *Observational evidence for the two phases in Katrina*

On 27 August, the National Hurricane Center reported an ERC in Hurricane *Katrina* (Knabb *et al.*, 2006). However, we show here evidence that the evolution of the structure of Hurricane *Katrina* resembles a vacillation cycle.

Microwave and infrared satellite images of Hurricane *Katrina* are shown in Figure 5 for 0700 UTC (left panels) and 1530 UTC (middle panels) on 27 August and 0000 UTC on 28 August (right panels). These times are identified by Knabb *et al.* (2006) as being prior to, during and after the ERC, respectively. At 0700 UTC on 27 August, both cloud-top brightness temperature (Figure 5(a)) and low-level convection seen in the microwave image (Figure 5(d)) exhibit a ring-like structure of relatively even distribution of brightness temperature. This structure resembles the symmetric phase of the modelled vortex. On the other hand, at 1530 UTC on 27 August a highly asymmetric structure with a seemingly broken eyewall is evident with regions of cold cloud-top on the eastern side of the vortex centre (Figure 5(b)) and strong low-level convection in the sourthern part of the eyewall (Figure 5(e)). This structure is similar to the asymmetric phase of the simulated hurricane. Furthermore, Hurricane *Katrina* became symmetric again at 0000 UTC on 28 August with a ring-like eyewall (Figure 5(c) and (f)). Note that low-level convection within the eyewall became more evenly distributed, but with lower maximum intensity than during the previous time (compare Figure 5(e) and (f)).

The evolution of the structure of Hurricane *Katrina* during this period as described above is consistent with a vacillation cycle, in which the vortex changes from a symmetric phase to an asymmetric phase and back to a symmetric phase. Note that although the asymmetric phase appears to be similar to the broken-eyewall stage during an ERC, they are essentially different. The strong convection embedded within the eyewall during the asymmetric phase (Figure 5(e)) suggests that the breaking of the eyewall is not due to the weakening of the convection in the inner eyewall with the emergence of the outer eyewall as during an ERC.

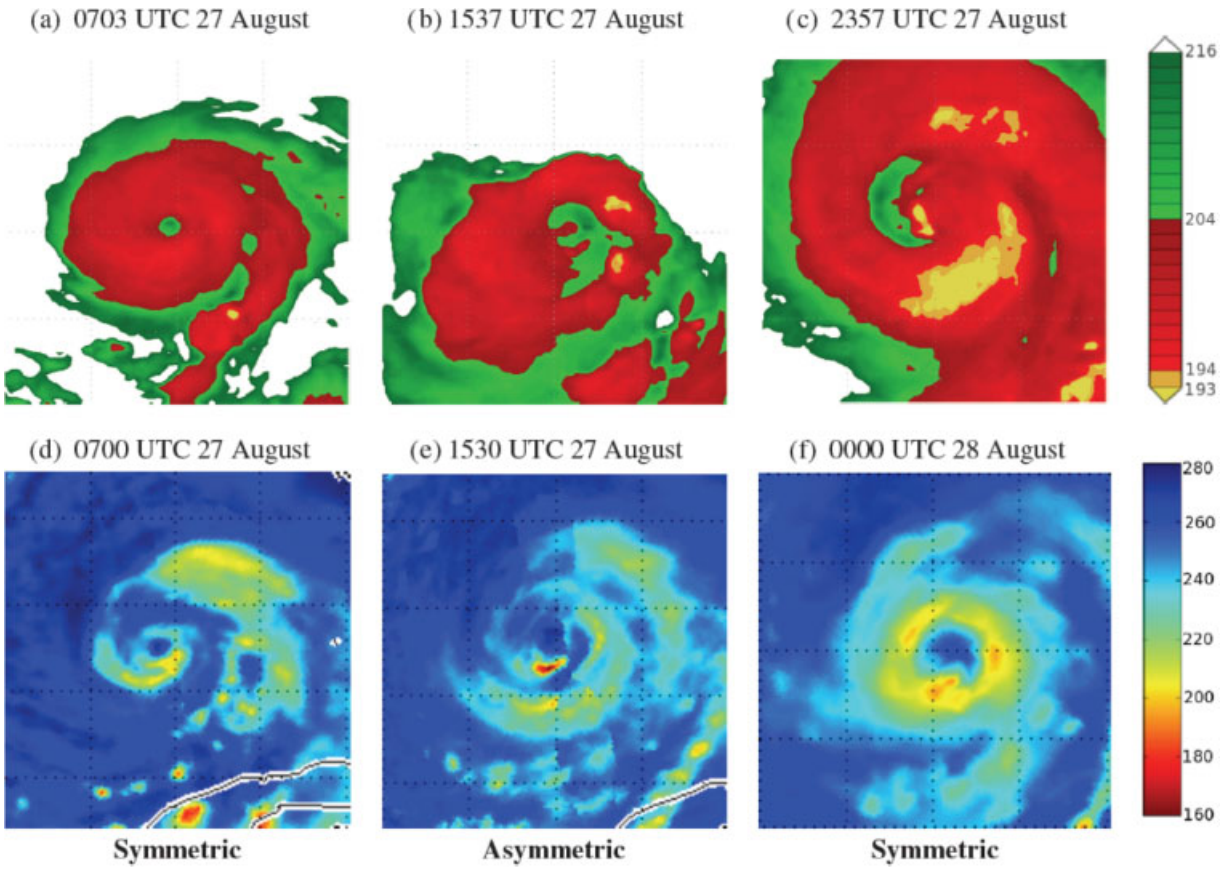

Figure 5. Brightness temperature [K] from satellite images of Hurricane *Katrina*. Top panels show infrared (IR) images from polar-orbiting satellites (Zehr, 2006) (data courtesy of Tropical Cyclone Polar Image Archive, Cooperative Institute for Research in the Atmosphere (CIRA)). Bottom panels show microwave images MIMIC (Wimmers and Velden, 2007) (images courtesy of University of Wiscosin/CMSS). Note that the times of IR and microwave images are close but do not match exactly, due to the availability of satellite data. (a) 0703 UTC on 27 August, (b) 1537 UTC on 27 August, (c) 2357 UTC on 27 August, (d) 0700 UTC on 27 August, (e) 1530 UTC on 27 August, (f) 0000 UTC on 28 August. Left and right panels are for the symmetric phase, centre panels are for the asymmetric phase. This figure is available in colour online at wileyonlinelibrary.com/journal/qj

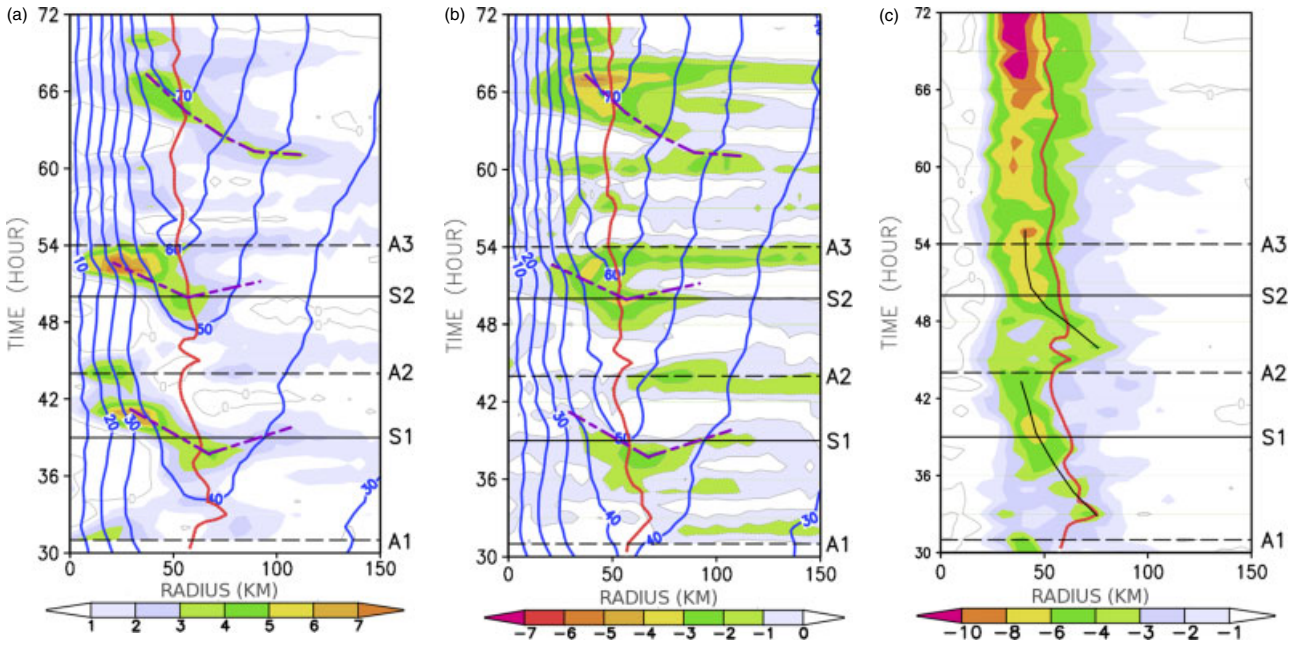

Figure 6. Radius–time plots of (a) tendency of the mean tangential wind $\partial\overline{v}/\partial t$ [m s^{-1} h^{-1}] (shaded) at 850 hPa; (b) tendency of the mean radial wind $\partial\overline{u}/\partial t$ [m s^{-1} h^{-1}] (shaded) at 900 hPa; (c) mean vertical velocity $\overline{\omega}$ [Pa s^{-1}] at 850 hPa. In (a) and (b), solid contours (blue in the online article) show the mean tangential wind $\overline{v}$ [m s^{-1}] at the corresponding levels, while dashed tilted lines (purple in the online article) indicate the axes of maximum $\partial\overline{v}/\partial t$ at 850 hPa. Bold solid lines (red in the online article) in (a), (b) and (c) show the RMW at the corresponding levels. Two curved solid black lines in (c) mark the axes of maximum $\overline{\omega}$. This figure is available in colour online at wileyonlinelibrary.com/journal/qj

3.3. *Evolution of the mean fields*

The relationship between the rates of intensification (discussed in section 2) and the azimuthal mean fields are examined now.

3.3.1. *Tangential and radial winds*

Figure 6(a) shows radius–time plots of the isotachs of azimuthal-mean tangential wind at 850 hPa and its tendency. During the symmetric phases, the region of maximum $\partial\overline{v}/\partial t$ occurs near the radius of maximum azimuthal-mean tangential wind (RMW). This region moves inwards during the transition towards the subsequent asymmetric phase and is thus consistent with the variation of intensification rate, $\partial\overline{v}_{\max}/\partial t$, with time as described in section 2 of this article. The rate at which $\overline{v}_{\max}$ intensifies during the asymmetric phase is slow because the largest acceleration occurs at inner radii instead of at the RMW as during the symmetric phase. The strong acceleration of $\overline{v}$ at inner radii and weak acceleration or deceleration near the RMW during the asymmetric phase can be understood by stirring effects induced by local circulations of the VHTs, which are strongest during this phase. Fast-moving air near the RMW is mixed with the slower-moving air at inner radii, thereby leading to a large acceleration at inner radii and a smaller acceleration near the RMW.

Figure 6(a) also shows regions of weak acceleration of $\overline{v}$ in a large area at outer radii during the asymmetric phases (e.g. from 60–120 km during A2). The increase of $\overline{v}$ at these radii can be explained through the effects of VHTs in producing near-surface, system-scale convergence. In an azimuthally-averaged sense, this air partially conserves its absolute angular momentum and spins faster. Indeed, Figure 6(b), which shows the acceleration of the mean radial wind $\partial\overline{u}/\partial t$ at 900 hPa (which is within the boundary layer),[§] has corresponding regions of accelerating radial inlow ($\partial\overline{u}/\partial t < 0$) at outer radii during the asymmetric phases (see e.g. the shaded region from 60–150 km radius during A2). Likewise, the acceleration of $\overline{v}$ near the RMW during the symmetric phases coincides with the acceleration of $\overline{u}$ in the boundary layer.

Figure 6(a) and (b) indicates that there are two processes increasing $\overline{v}$ at 850 hPa. In addition to the direct stirring effects of the VHTs, which lead to a strong acceleration of $\overline{v}$ at radii well inside the RMW during the asymmetric phase, there is a second mechanism for spin up that operates during both phases. This process is associated with acceleration of the radial inflow near the top of the boundary layer, which leads to the strengthening of $\overline{v}$ near the RMW during the symmetric phase and at outer radii during the asymmetric phase.

3.3.2. *Vertical velocity*

The vacillation of the azimuthal-mean vertical velocity $\overline{\omega}$, shown in Figure 6(c), is similar to that found in ERCs. For example, prior to symmetric phase S1 the mean eyewall moves inwards (solid black lines mark this inward movement). During the asymmetric phase (e.g. A2), the inner eyewall weakens while the strongest upward motion develops at some outer radius, similar to the formation of the outer eyewall during ERCs. Subsequently, this region of strong convection contracts, again reminiscent of a typical ERC. The intensity changes during the vacillation cycles are also analogous to those of ERCs. Specifically, the smaller intensification rates of the vacillation cycles during the asymmetric phase correspond to the slow intensification rates of hurricanes during the weakening of the inner eyewall in ERCs (Willoughby *et al.*, 1982). On the other hand, the symmetric phase of the vacillation cycles corresponds to the contraction phase of an ERC. Specifically, the breakdown of the eyewall during the asymmetric phase is not due to the formation of the outer eyewall as in ERCs. Rather, the eyewall breaks down as asymmetries develop within the eyewall itself (see e.g. Figure 3(a) and (d)), suggesting that these structure-change cycles are an alternative means for the inner core to intensify rapidly. Moreover, unlike ERCs, the vacillations are associated with episodic vortex-scale stirring.

3.3.3. *Potential vorticity*

The evolution of the radial gradient of the azimuthal-mean PV at 850 hPa, shown in Figure 7(a), illustrates the vacillation between ring and monopole structures, which characterize the symmetric and asymmetric phases respectively. The monopole structure has a negative radial gradient of PV at all radii from the vortex centre, whereas the ring structure has a positive radial gradient at inner radii and a negative radial gradient at outer radii. Thus regions with shaded values from the centre indicate a monopole structure and regions with blank areas near the centre changing to shaded at some particular radius indicate a ring structure. Monopole structures occur during the periods 30–38, 44–47 and 51–54 h, whereas ring structures are found during the intervening periods 38–44 and 47–51 h and after 54 h. These periods of monopole and ring structures (except for the times after 54 h) correspond to the symmetric and asymmetric phases described earlier in section 3.

A change in the sign of the mean PV gradient of the ring structure is a necessary condition for barotropic instability (Rayleigh, 1880; Schubert *et al.*, 1999) suggesting that the periods during which the vortex is in the symmetric phase are susceptible to barotropic instability. Thus the growth of VHTs, which heralds the end of the symmetric phase and the transition to the asymmetric phase, may be initiated and organized by this barotropic instability. The effects of the latter will be examined in the next section. However, during the mature stage (after 54 h of integration) the simulated vortex reaches a quasi-steady configuration in which the mean PV maintains a ring-like structure without vacillating between ring and monopole structures. The reasons why the vacillation ceases will be addressed in the next section.

3.3.4. *Equivalent potential temperature*

Figure 7(b) shows radius–time plots of azimuthal-mean θ_e at 850 hPa. Here, again the vacillation pattern is evident,

[§]In this study, the boundary layer is defined as the layer adjacent to the surface, where frictional drag reduces the absolute angular momentum and leads to strong radial inflow. The boundary layer is seen in vertical cross-sections as the layer within which the absolute angular momentum increases with height. With this definition, the 900 hPa level lies in the boundary layer and the 850 hPa level is just above the boundary layer.

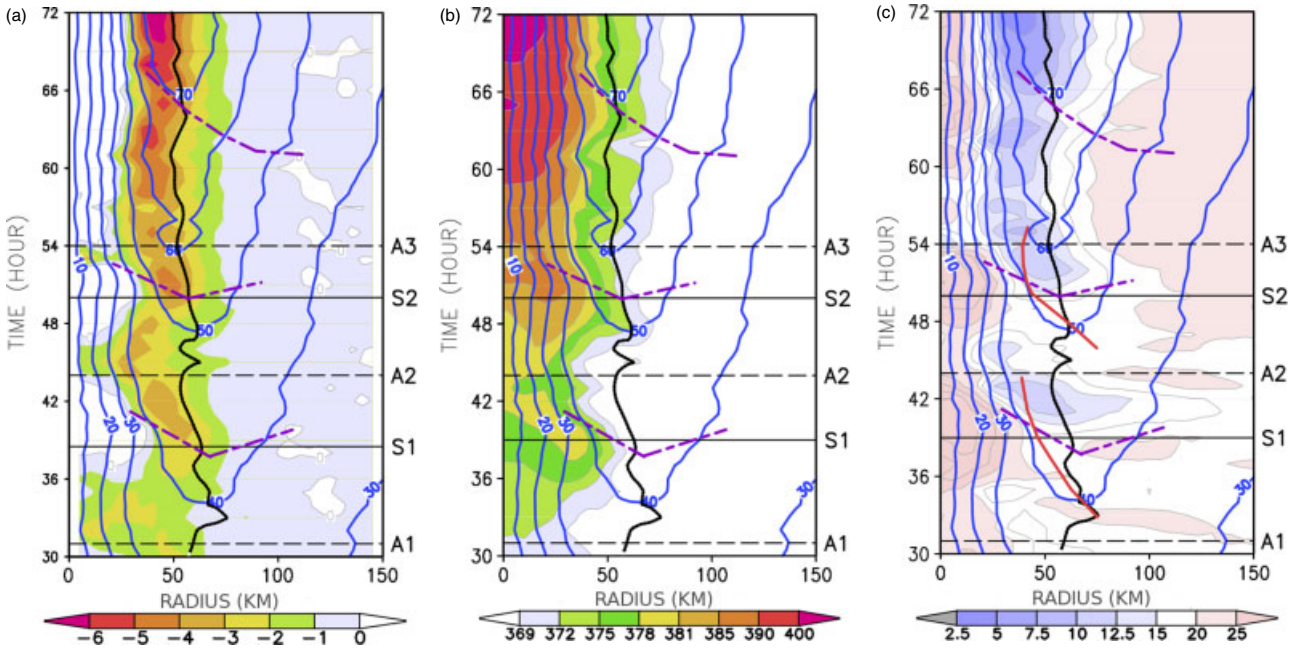

Figure 7. Radius–time plots for (a) radial gradient of mean PV $\partial\overline{PV}/\partial r$ [$10^{-4}\times$ PVU m^{-1}] at 850 hPa, with negative values shaded; (b) θ_e [K] at 850 hPa; (c) CAPE [$10^{-2}\times$J kg^{-1}]. Solid contours (blue in the online article) and dashed tilted lines (purple in the online article) show the same features as in Figure 6. Bold solid black lines show the RMW at 850 hPa. Two curved solid lines (red in the online article) in (c) mark the axes of maximum $\overline{\omega}$. This figure is available in colour online at wileyonlinelibrary.com/journal/qj

with a ring structure during the symmetric phase and a monopole structure during the asymmetric phase. During the symmetric phase, there is a ring of high θ_e at some radius (centred at 40 km during S1 and 25 km during S2). During the asymmetric phase, the θ_e field exhibits a maximum at the vortex centre and decreases significantly near the RMW.

An analysis of the terms in the tendency equation for θ_e, which was carried out in Nguyen (2010) (not shown), indicates that the high θ_e ring structure during the symmetric phase is due primarily to vertical advection of θ_e. On the other hand, the decrease of θ_e near the RMW during the asymmetric phase is accompanied by the horizontal advection of θ_e, which is consistent with the stirring effects of VHTs during this phase (as discussed earlier in Figure 4(f)).

3.3.5. *CAPE*

Convective Available Potential Energy (CAPE) and convection are highly interdependent. Increases in CAPE increase the intensity of convection, while, in turn, the convection consumes the CAPE and stabilizes the atmosphere. This negative feedback is demonstrated clearly in the evolution of the azimuthal-mean CAPE[¶] shown in Figure 7(c).

During the transition to asymmetric phases, the CAPE decreases substantially outside the axes of maximum $\partial\overline{v}/\partial t$ (dashed tilted straight black lines), which is where convection is most active. Just prior to the times of maximum asymmetry, regions of minimum CAPE coincide with the maximum updraught (two short solid curves, red in the online article), indicating that the convection consumes the CAPE.

Conversely, during the transition from the asymmetric to the symmetric phase, the CAPE near the RMW is restored to higher values (see regions near the RMW from A1–S1 and A2–S2). This increase in CAPE may be explained in part by fewer and weaker VHTs during this period, and in part by the increase of θ_e at low levels (see the above explanation of the ring structure in θ_e).

4. Transition mechanisms

4.1. *Symmetric to asymmetric transition*

This section examines the physical mechanisms that produce asymmetric structures and are responsible for the change from a symmetric to an asymmetric vortex.

4.1.1. *The role of barotropic instability*

Kossin and Eastin (2001) suggest that the transition from Regime 1 to Regime 2 (equivalent to the symmetric to asymmetric transition) is a consequence of barotropic instability. Their hypothesis is that the instability leads to the breakdown of the PV ring with the formation of mesovortices and that the accompanying mixing results in a monopole structure (Regime 2 or the asymmetric phase).
A difficulty with this argument is that the growth rate of barotropic disturbances appears to be too small to account for this regime transition. In the calculations presented by Schubert *et al.* (1999), the whole process, including the breaking down of the ring-like structure and the formation of the monopole, takes about 12 h. This time is much longer than both that observed by Kossin and Eastin (2001) (within

[¶]CAPE is computed as $\int_{p_{LNB}}^{p_{LFC}} R_d(T_v - T_{v,env})\,\mathrm{d}\ln p$ for an air parcel lifted from the surface. R_d is specific gas constant for dry air, LNB and LFC are the levels of neutral buoyancy and free convection, respectively, p is pressure and T_v and $T_{v,env}$ are virtual temperatures of the air parcel and environment, respectively. The calculation is based on script '`plotskew.gs`', which is available from http://www.iges.org/grads/gadoc/gadocindex (the Grid Analysis and Display System (GrADS) users community).

1–2 h) and that found in the present simulation (about 2–4 h). The growth rates of disturbances in the analytical model and numerical analogues thereof (Schubert *et al.*, 1999, sections 2 and 3) are dependent on the amplitude and width of the annulus, and therefore these growth rates and the corresponding life cycles may be faster. On the other hand, Schecter and Montgomery (2007) indicate that when the effects of cloudiness are accounted for, the predicted growth rates may be reduced, depending on the extent of cloudiness. In light of these results, barotropic instability calculations should give an upper bound on the linear growth rate, provided that they are carried out for the simulated profiles.

As a means of estimating the time-scale for barotropic instability in the present flow, we apply the linear stability analysis worked out by Weber and Smith (1993). This analysis determines the normal modes of the mean tangential wind profiles from the simulations using the non-divergent barotropic vorticity equation. Figure 8(a) illustrates the amplitude evolution of the azimuthal wave number 4 component of PV at 850 hPa along a 50 km radius circle (lines) and the *e*-folding times (columns) of the corresponding wave number calculated by Weber and Smith's method. Episodes in which the *e*-folding time is short (i.e. fast growth rates) occur just prior to the subsequent asymmetric phase, at which times wave amplitudes peak (e.g. during S1 from 36–39 h and symmetric phase S2 from 51–53 h). During the mature phase, the amplitudes of wave number 4 do not grow even though the necessary conditions for instability are satisfied (e.g. 66–68 h). This non-development is consistent with the results of Wang (2008), who found that wave numbers 4 and higher are damped effectively by rapid filamentation, which is typically strong during the mature stage. Figure 8(b) shows the linear barotropic *e*-folding times for wave numbers 1–6 during the symmetric phases S1 and S2. Wavenumber 4 has the shortest *e*-folding times (corresponding to the fastest growth rates) compared with the other wave numbers.

The calculated growth rates are slower, and the *e*-folding times longer, than the time taken for the vortex to change from the symmetric phase to the asymmetric phase in the simulation. However, these theoretical calculations are for the linear instabilities of an unforced barotropic vortex, whereas the simulation is baroclinic and includes a relatively sophisticated representation of the physical processes. Nonetheless, the agreement between the timing of the calculated fast growth rates and the simulated peaks in amplitude of the corresponding wave numbers suggests that barotropic instability may play a part in promoting asymmetries during the initial stage of the transition towards the asymmetric phase.

A complimentary approach is to examine the budgets of kinetic and potential energies for the mean flow and eddies (i.e. asymmetries). The analysis method is adopted from the work of Kwon and Frank (2008), wherein the full derivation of the equations can be found. The barotropic conversion rate, which comprises all terms that are present in the tendency equations for both the mean and eddy parts of the kinetic energy (but with opposite signs), has the

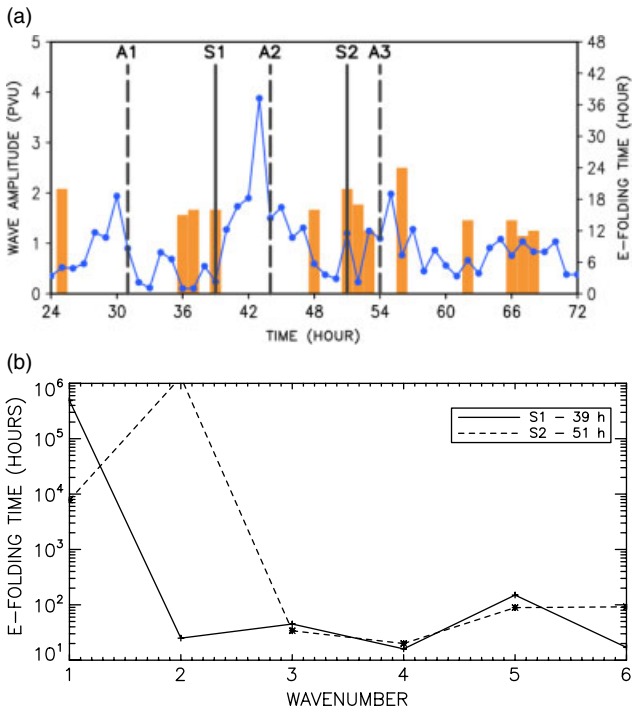

Figure 8. Linear barotropic growth rates. (a) Evolution of the amplitude of azimuthal wave number 4 calculated from PV (lines) at 850 hPa along the 50 km radius. The *e*-folding time [h] of perturbations imposed on the symmetric vorticity profiles of the simulated vortex is shown by columns. Here, *e*-folding times longer than 24 h are not plotted. Short columns indicate faster growth rates. (b) The *e*-folding times of wave numbers 1–6 during the symmetric phases S1 at 39 h (solid line) and S2 at 51 h (dashed line). This figure is available in colour online at wileyonlinelibrary.com/journal/qj

form

$$\left[\overline{u'u'}\frac{\partial \overline{u}}{\partial r} + r\overline{u'v'}\frac{\partial}{\partial r}\left(\frac{\overline{v}}{r}\right) + \overline{u'\omega'}\frac{\partial \overline{u}}{\partial p} + \overline{v'\omega'}\frac{\partial \overline{v}}{\partial p} + \frac{\overline{u}}{r}\overline{v'v'}\right]. \quad (1)$$

Here primes denote the deviations of the variables from their azimuthal means at each level. The radial, tangential and vertical wind components are u, v and ω, respectively, and, as before, p is the pressure. Positive conversion rates indicate that the kinetic energy of eddies is transferred to the kinetic energy of the mean flow.

Figure 9(a) shows the evolution of the vertical profile of the barotropic conversion rate averaged over radii from 10–100 km. After the symmetric phases S1 and S2, the barotropic conversion rate is negative (shaded with dark colour), indicating that the kinetic energy of the mean flow is converted into eddy kinetic energy, which is consistent with the idea that barotropic instability plays a role in the transition. Note that negative barotropic conversion rates occur also during periods other than the symmetric-to-asymmetric transition, and are especially noticeable after the asymmetric phase A3. Thus, barotropic energy conversion does not occur only during the symmetric-to-asymmetric transition.

4.1.2. *The role of convective instability*

We now present evidence suggesting that the development of VHTs plays an important role in the transition to

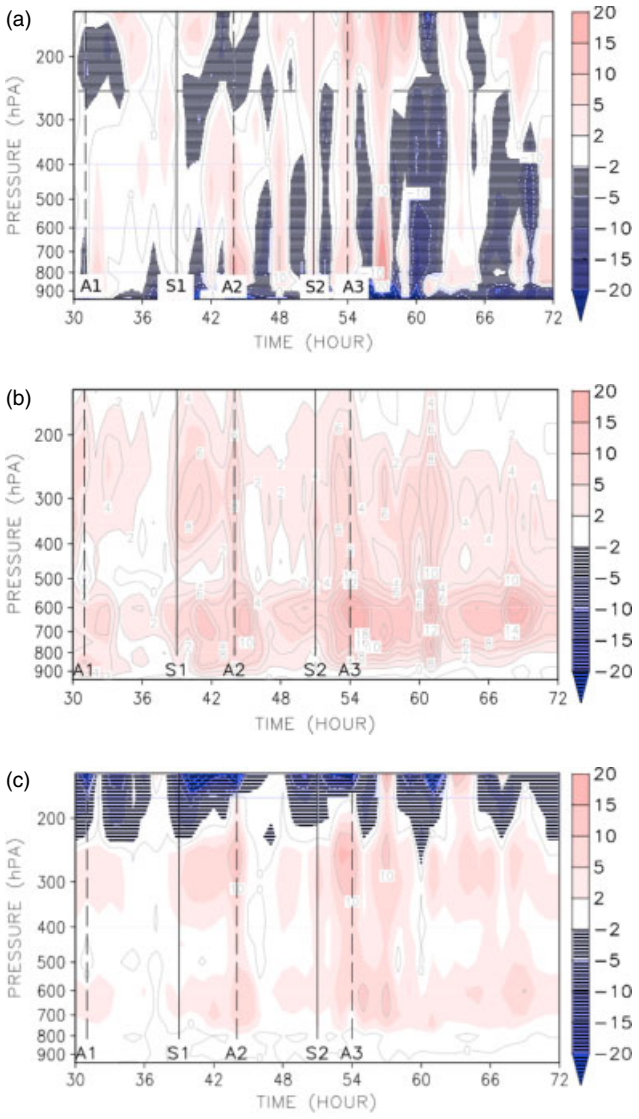

Figure 9. Evolution of energy conversion rates. (a) Barotropic conversion $[10^{-3} \times \mathrm{m}^2\,\mathrm{s}^{-3}]$ as in Eq. (1). (b) Convective conversion $-h\overline{\theta'\omega'}$ $[2 \times 10^{-3} \times \mathrm{m}^2\,\mathrm{s}^{-3}]$. (c) Baroclinic conversion $[10^{-3} \times \mathrm{m}^2\,\mathrm{s}^{-3}]$ as in Eq. (2). This figure is available in colour online at wileyonlinelibrary.com/journal/qj

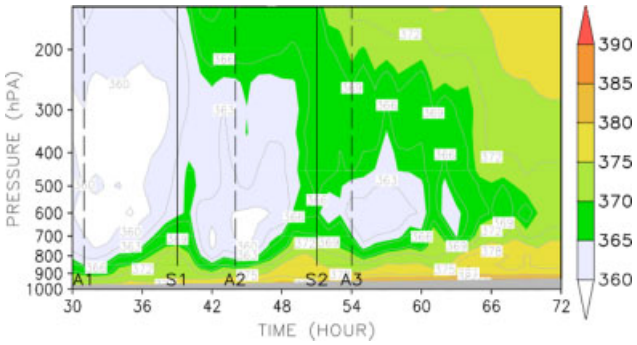

Figure 10. Evolution of the azimuthally-averaged θ_e [K] for radii between 40 and 60 km, encompassing the eyewall. This figure is available in colour online at wileyonlinelibrary.com/journal/qj

the asymmetric phase. Figure 10 shows the evolution of the vertical structure of θ_e near the eyewall. Low-level θ_e and hence convective instability increase as the vortex becomes more symmetric, reaching a maximum during the symmetric phase.

The transfer of eddy potential energy to eddy kinetic energy represents the effects of convection and is defined by $-h\overline{\theta'\omega'}$ (Kwon and Frank, 2008).[‖] The evolution of this term is shown in Figure 9(b). The term is positive throughout the integration, indicating that convective processes are (not surprisingly) active in the core region. Further, during the transition from the symmetric to asymmetric phase (e.g. from S1–A2 and from S2–A3), the convective conversion term increases in magnitude, reaching maxima at the times of maximum asymmetry (t_{A2}, t_{A3}).

[‖]Here $h = (R/p)(p/p_{\mathrm{ref}})^{(R/C_p)}$, $p_{\mathrm{ref}} = 10^5$ Pa, $R = 287\,\mathrm{J\,kg^{-1}\,K^{-1}}$ is the specific gas constant and $C_p = 1004\,\mathrm{J\,kg^{-1}\,K^{-1}}$ is the specific heat capacity of dry air.

4.1.3. *The role of baroclinic processes*

For completeness, Figure 9(c) shows the baroclinic energy conversion rate, which comprises all the terms that are present in the tendency equations for both the mean and eddy available potential energy:

$$\left[\left(\frac{h}{s}\right)^2 \overline{u'\theta'}\frac{\partial\overline{\theta}}{\partial r} + \left(\frac{h}{s}\right)^2 \overline{\omega'\theta'}\frac{\partial\overline{\theta}}{\partial p}\right], \qquad (2)$$

where $s^2 = -h(\partial\theta_0/\partial p)$ and θ_0 is the areal mean θ at each level (Kwon and Frank, 2008). Positive values of this term indicate the conversion from eddy potential energy to mean potential energy.

In Figure 9(c), the baroclinic energy conversion term is positive throughout the troposphere and has a larger magnitude during the symmetric-to-asymmetric transition, indicating that the potential energy of the eddies is transferred to mean potential energy. Thus, this process reduces the amplitudes of the eddies (i.e. the asymmetries), especially during the symmetric-to-asymmetric transition, while increasing the potential energy of the mean flow.

Note that the magnitudes of the barotropic and baroclinic conversion terms (Figure 9(a) and (c)) are smaller than the convective conversion term (Figure 9(b)), indicating the dominant role of convective processes.

4.1.4. *The formation of the monopole structure*

The effects of PV stirring during the asymmetric phase are now examined. Figure 11 shows the evolution of a local PV maximum identified by the Laplacian of PV ($-\nabla^2 PV$). Initially, the cyclonic PV anomaly (marked by a filled circle inside a triangle) is associated with a deep convective area (Figure 11(a)), but over the next 40 minutes it gradually detaches from the convective area (Figure 11(b), (c) and (d)) and moves towards the vortex centre (Figure 11(e) and (f)). The PV monopole structure with its maximum at the vortex centre develops through a sequence of similar episodic mixing events.

The movement of the local maxima of cyclonic PV towards the vortex centre can be explained by a process similar to the nonlinear β effect, which leads to a northwestward drift of tropical cyclones in the Northern Hemisphere and a southwestward drift in the Southern Hemisphere (see e.g. chapter 4 of Elsberry *et al.*, 1987). In the Northern Hemisphere, the advection of planetary vorticity by the

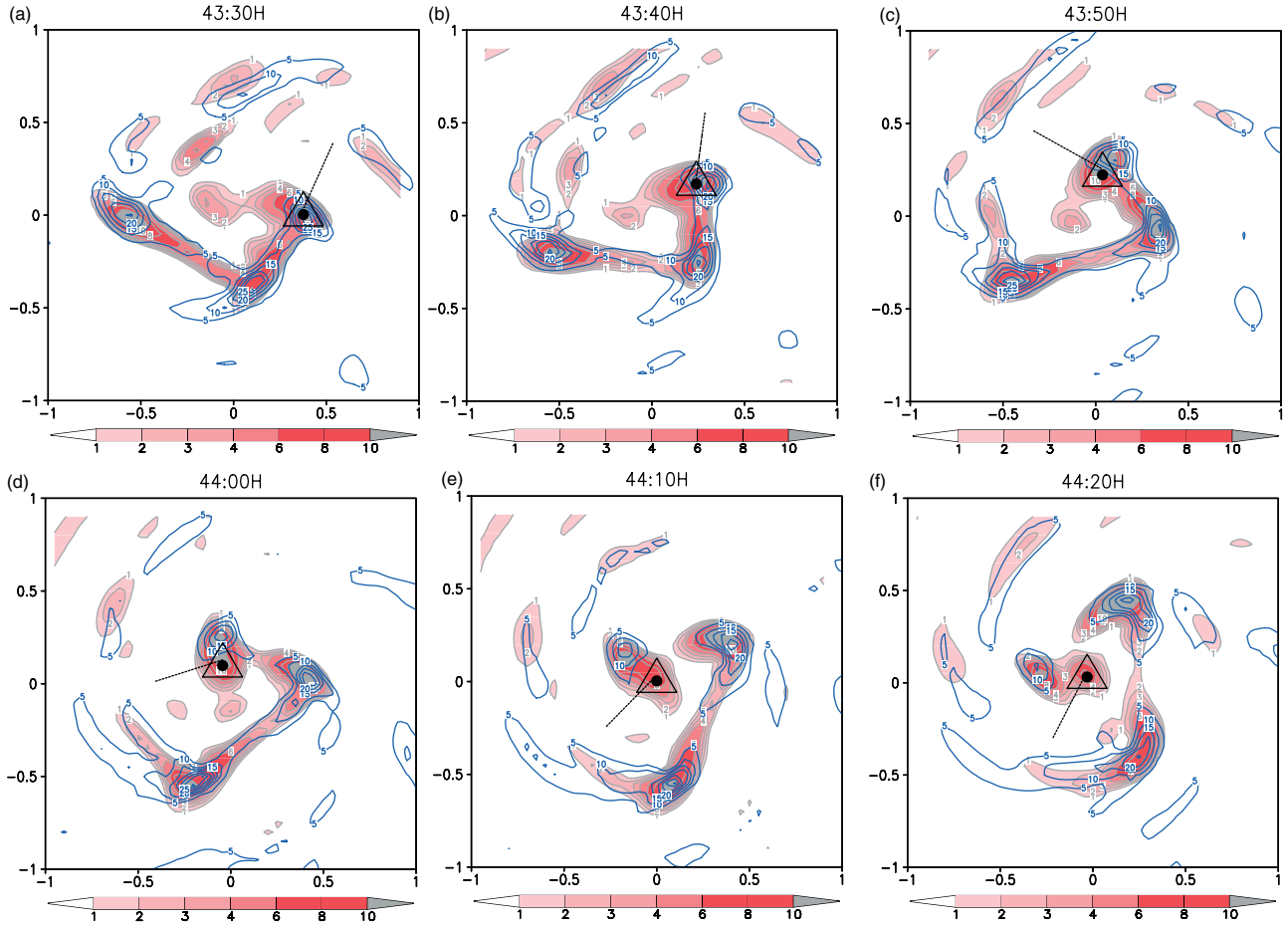

Figure 11. Local PV maxima at 850 hPa represented by $-\nabla^2(\mathrm{PV})$ [$10^{-8}\times$ PVU m^{-2}] (shaded regions represent positive anomalies). Labels on the horizontal and vertical axes show distance in degrees from the vortex centre in the zonal and meridional directions, respectively. Contours are vertical velocity in pressure coordinates [-1 Pa s^{-1}]. Dotted lines ending with filled circles inside triangles mark the positions of a tracked local PV maximum. The figures show the fields at 10 min intervals after 43:30 h of integration, during the transition from the symmetric to the asymmetric phase. (a) 43:30 h, (b) 43:40 h, (c) 43:50 h, (d) 44:00 h, (e) 44:10 h, (f) 44:20 h. This figure is available in colour online at wileyonlinelibrary.com/journal/qj

vortex circulation induces an anticyclonic tendency on the eastern side of the vortex and a cyclonic tendency on the western side. The ensuing vorticity-anomaly pattern is rotated by the cyclonic circulation of the vortex and leads to an induced flow across the vortex centre towards the northwest. This flow accounts for the northwestward drift of the vortex. In more complex flows, vortices tend to move with a component towards higher PV. In a barotropic context, the tendency for small-scale cyclonic vortices to migrate to the centre of larger ones was discussed by Ulrich and Smith (1991).

During the symmetric-to-asymmetric transition, a similar process occurs with VHTs, which are embedded in a negative radial gradient of azimuthal-mean PV (not shown here). Then, analogous to a vortex on a β plane, the VHTs move towards higher PV. During this inward movement, the VHTs stir** high PV near the eyewall and low PV within the eye, thereby increasing the PV near the vortex centre. For this reason, the central pressure falls most rapidly during the asymmetric phases (Figure 2), as the PV accumulates at the vortex centre.

As the VHTs move inwards into a region with warm air aloft, the convection decays due to the decreased static instability. However, the low-level PV anomalies they produce outlive the updraughts and continue moving inwards. These PV anomalies, which are not accompanied by deep convection, appear to be what was described previously in the literature as eyewall mesovortices (Kossin *et al.*, 2002). These mesovortices have been interpreted as originating from barotropic instability (Kossin *et al.*, 2000; Kossin and Schubert, 2001). We have shown here that mesovortices may originate from VHTs in this case.

In summary, the symmetric-to-asymmetric transistion is accompanied by the development of VHTs within the eyewall. The VHTs are formed as a result of a combination of barotropic and convective instabilities, which can be termed as 'barotropic–convective instability'. Subsequently, the low-level cyclonic PV anomalies associated with the VHTs move towards the centre, leading to the formation of a monopole during the asymmetric phase.

4.2. *Asymmetric to symmetric transition*

In contrast to the symmetric-to-asymmetric transition, during which VHTs grow within the eyewall, the VHTs weaken during the asymmetric-to-symmetric transition. After the times of maximum asymmetry, they become

**Although the physical size of VHTs appears to be small (of the order of 10–20 km), the advection by their circulations (as determined in budget calculations which are not shown here for brevity) affect much larger surrounding areas (of the order of 50 km).

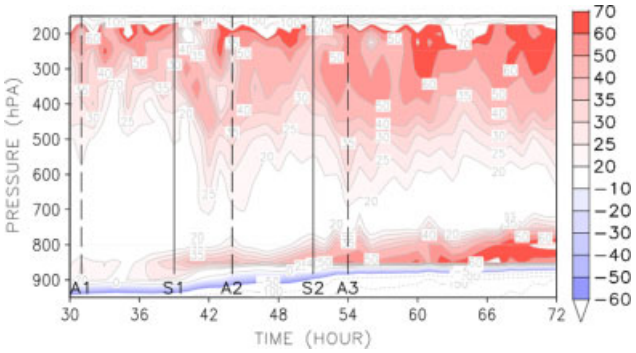

Figure 12. Evolution of the vertical gradient of the mean tangential wind $\partial\overline{v}/\partial p$ $[10^{-5}\times \mathrm{m\,s^{-1}\,Pa^{-1}}]$ averaged across the eyewall region (from 10–50 km). This figure is available in colour online at wileyonlinelibrary.com/journal/qj

elongated convective bands moving outwards and more slowly azimuthally than the azimuthal-mean tangential wind. This outward and retrogressive movement is similar to that of VRWs and is to be expected, since the radial gradient of azimuthal-mean PV is negative. At the same time, the associated large rate of strain at the peripheries of the VHTs (see Figure 7(c) and (d)) also weaken, thereby producing an environment more favourable for the development of convection at outer radii.

The section below examines the reasons why the VHTs weaken, the similarity of the convective bands to VRWs and the relationship between the rate of strain and convection at outer radii.

4.2.1. *The role of local vertical shear*

The reduction of CAPE (Figure 7(c)) is not the only process weakening VHTs after the asymmetric phase. The evolution of the local vertical wind shear in the eyewall region also plays a role.

The decrease of the cyclonic tangential wind with height (which is a signature of warm-cored systems) creates an environment unfavourable for the development of deep convection: while the lower part of a VHT is embedded in the rapidly rotating flow in the lower troposphere, its upper part may encounter much slower cyclonic rotation. As a result, VHTs in such an environment will be tilted backwards (i.e. upstream) with height, leading to a weakening of the convection. As a first step to examining this effect, we now investigate the evolution of the vertical gradient of azimuthal-mean tangential wind.

Figure 12 shows the evolution of the vertical gradient of mean tangential wind near the eyewall (averaged over 10–50 km radii) where the VHTs are located. The vertical shear of azimuthal-mean tangential wind in the middle and upper troposphere (shaded regions above the 700 hPa level) increases noticeably towards the asymmetric phase, as the vortex spins up at low levels. This increase of the mean tangential wind at low levels is a result of horizontal stirring by the VHTs, the horizontal influx of mean absolute vorticity and the vertical advection of azimuthal momentum by the mean overturning circulation. The resulting increase in the vertical shear of the azimuthal-mean tangential wind that develops in advance of the asymmetric phase, reaching a maximum when the vortex is most asymmetric, creates a less favourable environment for convection.

4.2.2. *Vortex Rossby waves*

VRWs have been proposed as an asymmetric mode of intensification (Montgomery and Kallenbach, 1997; Möller and Montgomery, 1999, 2000) and are associated with PV asymmetries. These asymmetries are typically created by convection, often in the form of inner spiral rain bands. In the environment of the vortex's mean negative radial PV gradient, positive PV anomalies tend to move radially outwards and, while they move cyclonically, they retrogress relative to the mean tangential wind. As they move outwards, these PV anomalies experience strong straining by the differential rotation of the mean tangential flow; they become narrower and their radial wave number increases. Thus, according to the dispersion relation derived by Montgomery and Kallenbach (1997), the radially outward group velocity decreases and there may exist a critical radius at which the group velocity becomes zero. At this radius, the disturbance gives its energy to the mean flow (Montgomery and Kallenbach, 1997; Möller and Montgomery, 1999, 2000).

In the simulation described herein, the weakened VHTs become stretched bands of moderate convection moving outwards, thus, resembling VRWs. The phase and group propagation speeds of the theoretical VRWs are computed using the formulae of Möller and Montgomery (2000) (for constant radial wave numbers). Figure 13 shows an azimuthal Hovmöller diagram of vertical velocity (shaded) overlaid with the PV along the 50 km radius circle. The VHTs, as marked by strong upward motion and positive PV anomalies, are tracked and their azimuthal speeds are compared with the theoretical phase speeds of VRWs. These calculations are carried out using the azimuthal-mean profiles of tangential wind speed, PV, and static stability at 850 hPa of the simulated vortex for disturbances having azimuthal wave numbers of 2, 3 or 4. The radial and vertical wave numbers are chosen arbitrarily for waves having length-scales of 50 km and 10 km in the respective directions. Whether or not the entities tracked can be considered VRWs can be judged by the degree to which the measured and theoretical speeds agree.

In Figure 13, the tracked VHTs (marked by black long-dashed lines) move more slowly than both the mean flow (solid lines) and the calculated phase speeds of VRWs (long–short-dashed lines, blue in the online article). This retrogression of the VHTs is pronounced during the symmetric-to-asymmetric transition (see, for example the large angle marked by (*) near 41 h and an azimuth of 310° during the transition from S1 to A2) while the VHTs are strengthening. In contrast, after the asymmetric phase A2, the weakening VHTs move with nearly the theoretical VRW speeds, which predict small retrogression relative to the mean flow (see below).

The retrogression of the VHTs is illustrated more clearly in Figure 14. During the symmetric phases (e.g. S1 at 39 h and S2 at 50 h), the average retrogression of the tracked VHTs is of the order of 30%, whereas just after the asymmetric phase A2 near 44–45 h it drops to around 10%, close to the theoretical estimates. To the extent that this retrogression is a signature of VRWs, the tracked convective entities behave more like VRWs during the asymmetric-to-symmetric transition than during the symmetric-to-asymmetric transition.

Figure 15 shows the theoretical radial phase and group speeds of the VRWs. The propagation of these waves is

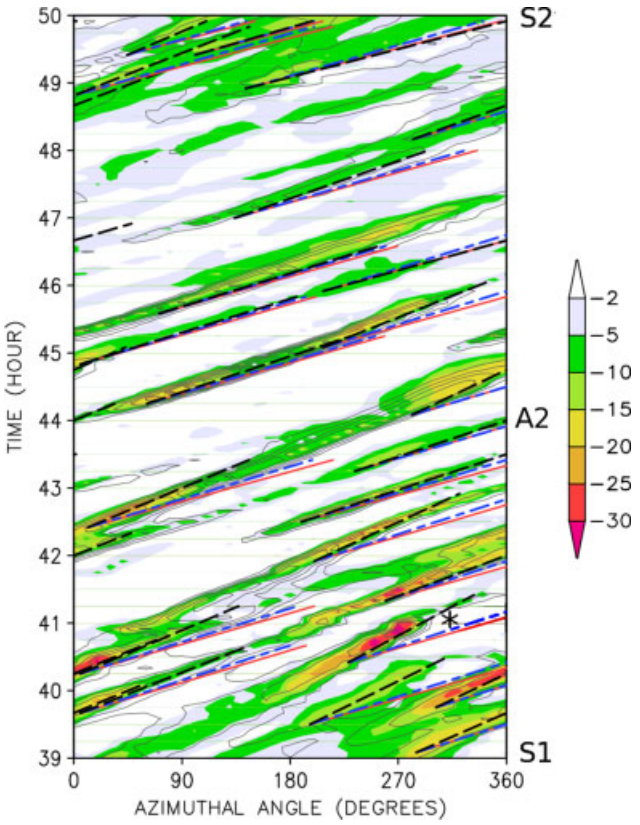

Figure 13. Hovmöller diagram of vertical velocity (shaded) and PV (contour) at 850 hPa along the 50 km radius circle. On the horizontal axis, the direction from left to right is cyclonic displacement. Solid straight lines (red in the online article) are the direction of movement with the mean tangential flow. Long-dashed (black) lines indicate the movement directions of the tracked VHTs. Long–short-dashed lines (blue in the online article) show movement with theoretical VRW phase speeds for the azimuthal wave number 3. Note that PV contours are not the main focus of this plot, but are shown to illustrate the typical collocation of updraughts and positive PV anomalies within VHTs. This figure is available in colour online at wileyonlinelibrary.com/journal/qj

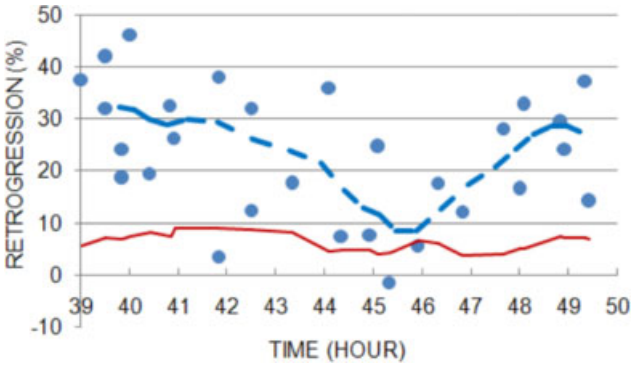

Figure 14. Retrogression calculated by $(\overline{v} - c)/\overline{v} \times 100\%$ (circles) of tracked VHTs and the calculated VRW phase speed for wave number 3 (solid thin line, red in the online article). The dashed line (blue in the online article) represents the smoothed average retrogression of the tracked convective entities. c is the tangential speed of the VHTs. This figure is available in colour online at wileyonlinelibrary.com/journal/qj

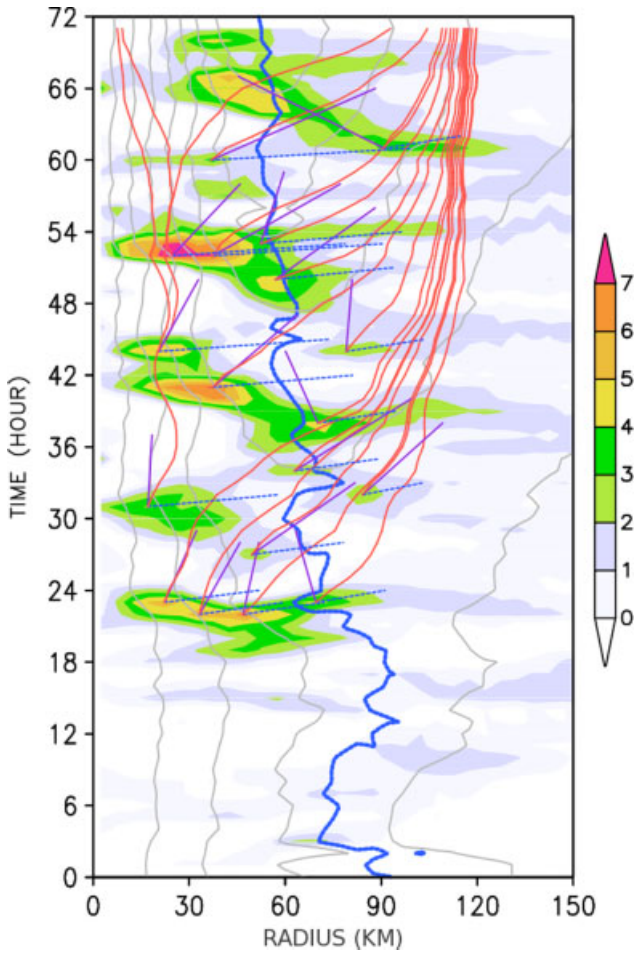

Figure 15. Radial phase (Cp_r) and group (Cg_r) speeds of theoretical VRWs for azimuthal wave number 3. The shaded areas show positive tendencies of $\overline{v}$ at 850 hPa. Contours show $\overline{v}$. The bold line (blue in the online article) represents the RMW. Solid thin curves (red in the online article) show radial propagation with radial group speed Cg_r, dashed straight lines (blue in the online article) are for radial phase speed Cp_r and solid straight lines (purple in the online article) illustrate the mean radial wind at each point of interest. This figure is available in colour online at wileyonlinelibrary.com/journal/qj

superimposed on the tendencies of the azimuthal-mean tangential wind in Figure 6(a) to identify any connection between the VRWs and changes in the mean tangential flow. According to Montgomery and Kallenbach (1997) and Montgomery and Enagonio (1998), the VRWs interact with the mean tangential flow where the group speed vanishes. In the simulation, the critical radius is near 120 km, where traces of the radial group propagation (thin solid curves in Figure 15, red in the online article) converge. However, there does not seem to be any significant increase in the mean tangential wind at the critical radius, indicating that wave–mean-flow interaction is weak at best.

4.2.3. *The reduced rate of strain at outer radii*

As shown in Figure 4(e) and (f), the rate of strain and thus the strain-dominated region just outside the RMW are more pronounced during the asymmetric phase than during the symmetric phase. As pointed out by Rozoff *et al.* (2006), the flow in such regions suffers rapid filamentation, which is unfavourable for the development of convection if the filamentation time-scale τ_{fil} (defined in section 1) becomes smaller than the convective time-scale. We show now that this is indeed the case, by examining the evolution of the filamentation time-scale in relation to the vertical motion in the region immediately beyond the RMW.

Figure 16 shows the evolution of the filamentation time-scale τ_{fil} and the azimuthal-mean vertical velocity in pressure coordinates $\overline{\omega}$ at 80 km radius at 850 hPa. This radius is

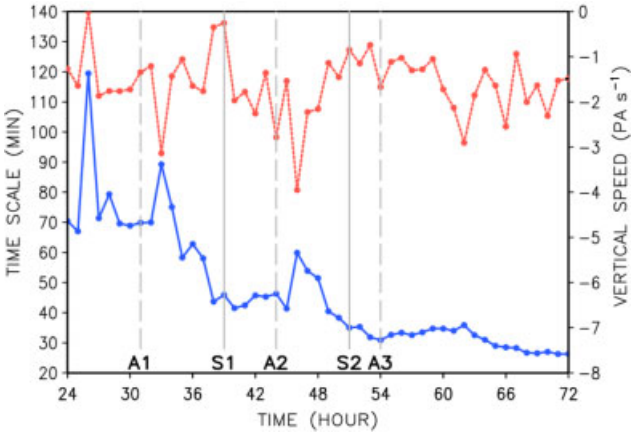

Figure 16. The evolution of the azimuthal-mean vertical velocity $\overline{\omega}$ [Pa s^{-1}] (dashed line, red in the online article) and azimuthal-mean filamentation time-scale $\overline{\tau_{\text{fil}}}$ [min] (solid line, blue in the online article) at the 80 km radius at 850 hPa. This figure is available in colour online at wileyonlinelibrary.com/journal/qj

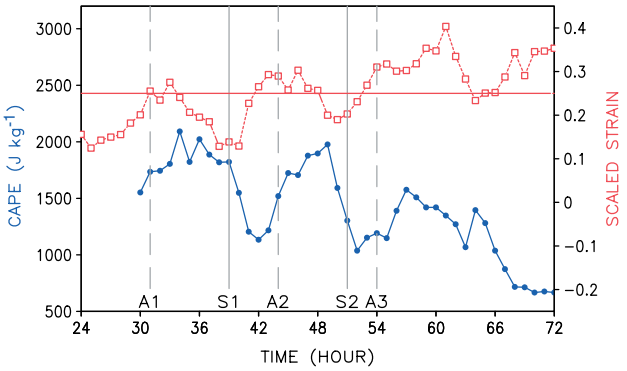

Figure 17. Evolution of azimuthal-mean CAPE (solid line with filled circles) [J kg^{-1}] and rate of strain scaled by relative vorticity $\gamma = S/\zeta$ (dashed line with squares) at a radius of 50 km. This figure is available in colour online at wileyonlinelibrary.com/journal/qj

always outside the RMW. As the vortex intensifies, the filamentation time-scale broadly decreases, although during the vacillation cycles there are sharp increases shortly after the times of maximum asymmetry (e.g. at 32 h after the asymmetric phase A1 and 46 h after the asymmetric phase A2 in Figure 16). Higher values of τ_{fil} correspond with a lower rate of strain and consequently a slightly more favourable environment for convection. Accordingly, the mean upward motion increases ($\overline{\omega}$ becomes more negative) during these times.

The development of convection beyond the RMW (e.g. at 80 km) and its subsequent inward movement resembles the development of a secondary eyewall during an ERC (see Figure 6(c) and the discussion thereof). Note that during the asymmetric-to-symmetric transition, all conditions for the formation of a secondary eyewall as hypothesized by Terwey and Montgomery (2008) are satisfied. These conditions include (1) reduced strain, (2) a moderately negative PV gradient (see Figure 7(a)) and (3) relatively high CAPE (in the order of 2000 J kg^{-1}, see Figure 7(c)). While the vacillation cycles identified here are different from the ERCs, the convective development beyond the RMW in the former may be similar to the formation of the secondary eyewall in the latter.

4.3. *The mature stage*

The vacillation cycles cease as the tropical cyclone reaches maturity, even though the conditions necessary for barotropic instability may remain satisfied. For example, there is a persistent region in which the PV gradient changes sign after the asymmetric phase A3 in Figure 7(a), and there are short *e*-folding times during 66–69 h in Figure 8(a). The reasons for this cessation are examined now.

Figure 17 shows the evolution of the azimuthal-mean CAPE (solid line with filled circles) at a radius of 50 km, which is near the eyewall. Despite large fluctuations during the vacillation cycles (a manifestation of the interdependent relationship between convection and CAPE as discussed earlier), the mean tendency of the CAPE is to decrease, reaching values of the order of 500 J kg^{-1} after 66 h. Consequently, the eyewall region during the mature stage is not favourable for very strong convection and the development of VHTs. As convective instability plays an important part in the development of asymmetries during the symmetric-to-asymmetric transition of the vacillation cycles, its reduction during the mature stage explains, in part, the cessation of the vacillation.

The enhanced rate of strain also appears to play a part in suppressing the vacillation during the mature stage. As shown by Dritschel *et al.* (1991), a rate of strain scaled by a relative vorticity as small as 0.25 may be enough to suppress conventional barotropic instability and thus prevent a strip of enhanced vorticity from breaking into a series of vortices. Although the configuration of the PV ring in tropical cyclones is different from the straight vorticity strip investigated by Dritschel *et al.*, their finding must apply, to some degree, to tropical-cyclone vortices.

The dashed line in Figure 17 shows the evolution of the scaled azimuthally-averaged rate of strain $\gamma = S/\zeta$ at a radius of 50 km. During the integration, although the rate of strain fluctuates strongly because of the vacillation of convection in this area, it increases on average. After the last asymmetric phase A3, the scaled rate of strain mostly maintains values above the threshold of 0.25 (marked by the horizontal dashed line in Figure 17). Thus, a scaled rate of strain in excess of 0.25 appears to explain the absence of vacillation cycles.

Figure 18 shows the fields of PV and rate of strain at 850 hPa and CAPE during the mature stage at 72 h. These fields illustrate the above-mentioned features. The structure of the PV in Figure 18(a) exhibits a complete ring of high PV centred near 30 km radius. High rates of strain, shown in Figure 18(b), are found just outside the 50 km radius and the values of CAPE within the eyewall are as low as 500 J kg^{-1} (Figure 18(c)). This configuration of the vortex inner core is unfavourable for vacillation cycles for the reasons discussed above.

5. Conclusions

It has been shown that, during the intensification stage, the structure of the modelled Hurricane *Katrina* vacillates between a more symmetric phase and a more asymmetric phase. The symmetric phase is characterized by a ring-like structure in the low-level PV and θ_e fields, and is accompanied by a rapid acceleration of the maximum azimuthal-mean tangential wind. In contrast, during the

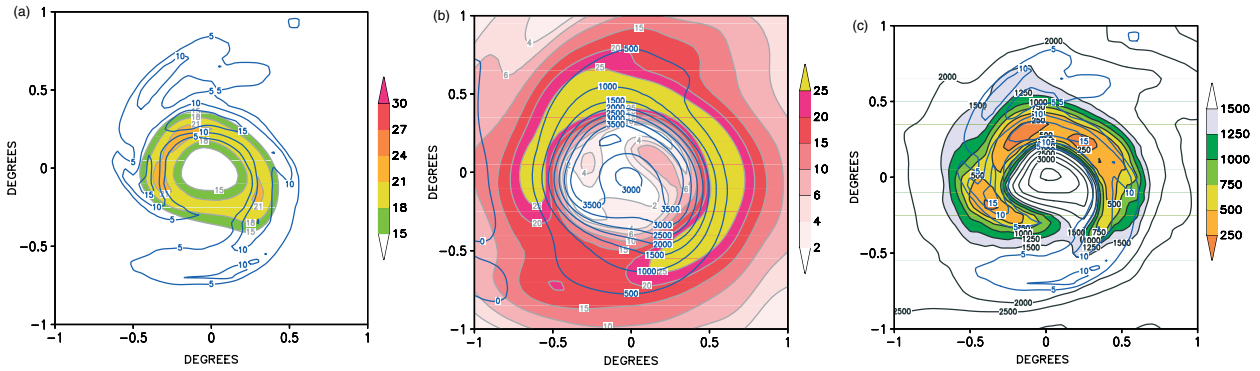

Figure 18. Vortex structure at 850 hPa during the mature stage at 72 h. Units of the displayed properties in panels (a) and (b) are the same as in Figures 3(d) and 4(f), respectively. In panel (c), regions with CAPE values lower than 1500 J kg^{-1} are shaded, bold (blue in the online article) contours show vertical velocity [−Pa s^{-1}] and thin (black) contours show CAPE values. (a) Potential vorticity, (b) rate of strain and (c) CAPE. This figure is available in colour online at wileyonlinelibrary.com/journal/qj

asymmetric phase the low-level PV and θ_e fields exhibit a monopole structure, with the corresponding maximum at the vortex centre. The asymmetric phase is accompanied by relatively low intensification rates of the azimuthal-mean tangential wind. These two phases are very similar to the two observed regimes reported by Kossin and Eastin (2001), the symmetric phase to their Regime 1 and the asymmetric phase to their Regime 2. A structural change resembling the modelled vacillation cycle is supported by satellite images of Hurricane *Katrina*.

While Kossin and Eastin (2001) propose barotropic instability as an explanation for the transition from Regime 1 to Regime 2, the model results presented here suggest that convective instability couples with the barotropic modes and significantly augments the growth rates. This hybrid instability is an efficient pathway to converting eddy diabatic heating to eddy potential energy. Moreover, a number of previously identified processes in the inner core of the tropical cyclone appear to play roles during the vacillation.

(1) During the *symmetric-to-asymmetric* transition, the release of barotropic–convective instability promotes asymmetries within the eyewall in the form of VHTs. These VHTs effectively stir vorticity and equivalent potential temperature between the eye and the eyewall, bringing the vortex to an asymmetric state with a monopole structure. Consistent with the vorticity arguments of Schubert *et al.* (1999), which highlight the spin-up of the eye region during these mixing episodes, the minimum pressure falls most rapidly during the asymmetric phase.

(2) The *asymmetric-to-symmetric* transition is accompanied by a weakening of the VHTs as the convective instability is exhausted and the local vertical wind shear increases. The weakened VHTs become stretched bands of moderate convection and move outwards as VRWs, which become more axisymmetrized in a strongly sheared mean flow. During this time, convection develops beyond the RMW in a region of reduced strain and high convective instability. This new region of outer convection moves inwards towards the RMW, resembling the contraction of the secondary eyewall in ERCs.

At later times during the mature stage, these vacillation cycles, including the breakdown of the eyewall into asymmetries, are not observed, despite the necessary Rayleigh condition for barotropic instability being satisfied. This suppression may be the result of the strong damping effect of large strain rates and rapid filamentation near the RMW. Moreover, as the CAPE near the eyewall is relatively low (smaller than 500 J kg^{-1}) at this time, the barotropic–convective instability mechanism appears to be suppressed.

These vacillation cycles are essentially different from ERCs. Specifically, the breakdown of the eyewall during the asymmetric phase is not due to the formation of the outer eyewall as is the weakening of the eyewall in ERCs. Rather, the eyewall breaks down as asymmetries develop within the eyewall itself, suggesting that these changes in structure are an alternative means for the inner core to intensify. Moreover, in contrast to ERCs, the vacillations are associated with episodic vortex-scale stirring. During an ERC, the inner eyewall weakens nearly uniformly in azimuth after the appearance of the outer eyewall. In contrast, during a vacillation cycle the eyewall breaks down into VHTs, followed by the development of convection beyond the RMW.

The picture to emerge from the model results is that vacillation cycles tend to occur during the intensification stage, before the vortex has developed into an adverse environment for both vortical convection and the growth of barotropic instability in the eyewall region. In other words, these vacillation cycles appear to be part of the intensification process in relatively young tropical cyclones. ERCs tend to occur in strong and mature hurricanes.

There is evidence of vacillation cycles in other simulations. In a complementary study, which will be published in due course, an ensemble of high-resolution simulations of Hurricane *Katrina* reveals that vacillation cycles are a robust feature that occurs in most ensemble members. Whether these vacillation cycles are a prevalent pathway to intensification in other models is a topic worthy of further research.

Acknowledgements

This work is a part of the PhD study of the first author, who was sponsored by an AusAID scholarship. The first author is grateful for travel support provided by Monash University as a European Travel Grant and the German Research Council (DFG) as part of the

Project 'Improved quantitative precipitation forecasting in Vietnam'. The code for calculation of barotropic instability was kindly provided by Dr Harry Weber. Satellite images were provided by Drs John Knaff and Ray Zehr, GOES Algorithm Working Group, Corporative Institute for Research in the Atmosphere, CIRA. The first author benefited greatly from helpful scientific discussions with Drs Kevin Tory, Jeff Kepert, Gary Dietachmayer, Lawrie Rikus, Greg Holland, John Knaff, James Kossin, Craig Bishop, Chris Snyder and Jun-Ichi Yano.

References

Black M, Burpee R, Marks F, Samsury C, Willoughby H. 2002. Eastern Pacific Hurricanes *Jimena* of 1991 and *Olivia* of 1994: The effect of vertical shear on structure and intensity. *Mon. Weather Rev.* **130**: 2291–2312.

Braun S, Montgomery MT, Pu Z. 2006. High-resolution simulation of Hurricane *Bonnie* (1998). Part I: The organization of eyewall vertical motion. *J. Atmos. Sci.* **63**: 19–42.

Davidson N, Puri K. 1992. Tropical prediction using dynamical nudging, Satellite-defined convective heat sources, and a cyclone bogus. *Mon. Weather Rev.* **120**: 2501–2522.

Davidson N, Weber H. 2000. The BMRC high-resolution tropical cyclone prediction system: TC-LAPS. *Mon. Weather Rev.* **128**: 1245–1265.

Dritschel D, Haynes P, Juckes M, Shepherd TG. 1991. The stability of a two-dimensional vorticity filament under uniform strain. *J. Fluid Mech.* **230**: 647–665.

Eliassen A. 1951. Slow thermally or frictionally controlled meridional circulation in a circular vortex. *Astrophysica Norvegica* **5**: 19–60.

Elsberry R, Frank W, Holland G, Jarrel J, Southern R. 1987. *A Global View of Tropical Cyclones*. Univ. of Chicago Press: Chicago, IL.

Guinn T, Schubert W. 1993. Hurricane spiral rainbands. *J. Atmos. Sci.* **50**: 3380–3403.

Hendricks E, Montgomery M, Davis C. 2004. On the role of 'vortical' hot towers in formation of Tropical Cyclone *Diana* (1984). *J. Atmos. Sci.* **61**: 1209–1232.

Knabb R, Rhome J, Brown D. 2006. '*Tropical cyclone report. Hurricane Katrina*', Technical Report. National Hurricane Center Available at www.nhc.noaa.gov/pdf/TCR-AL122005_Katrina.pdf.

Kossin J, Eastin M. 2001. Two distinct regimes in the kinematic and thermodynamic structure of the hurricane eye and eyewall. *J. Atmos. Sci.* **58**: 1079–1090.

Kossin J, Schubert W. 2001. Mesovortices, polygonal flow patterns, and rapid pressure falls in hurricane-like vortices. *J. Atmos. Sci.* **58**: 2196–2209.

Kossin J, Schubert W, Montgomery M. 2000. Unstable interactions between a hurricanes primary eyewall and a secondary region of enhanced vorticity. *J. Atmos. Sci.* **57**: 3893–3917.

Kossin J, McNoldy B, Schubert W. 2002. Vortical swirls in hurricane eye clouds. *Mon. Weather Rev.* **130**: 3144–3149.

Kwon Y, Frank W. 2008. Dynamic instabilities of simulated hurricane-like vortices and their impacts on the core structure of hurricanes. Part II: Moist experiments. *J. Atmos. Sci.* **65**: 106–122.

Möller J, Montgomery M. 1999. Vortex Rossby waves and hurricane intensification in a barotropic model. *J. Atmos. Sci.* **56**: 1674–1687.

Möller J, Montgomery M. 2000. Tropical cyclone evolution via potential vorticity anomalies in a three-dimensional balance model. *J. Atmos. Sci.* **57**: 3366–3387.

Montgomery M, Enagonio J. 1998. Tropical cyclogenesis via convectively forced vortex Rossby waves in a three-dimensional quasigeostrophic model. *J. Atmos. Sci.* **55**: 3176–3207.

Montgomery M, Kallenbach R. 1997. A theory for vortex Rossby waves and its application to spiral bands and intensity changes in hurricanes. *Q. J. R. Meteorol. Soc.* **123**: 435–465.

Montgomery M, Nicholls M, Cram T, Saunders A. 2006. A vortical hot tower route to tropical cyclogenesis. *J. Atmos. Sci.* **63**: 355–386.

Nguyen CM. 2010. '*Inner-core vacillation cycles during the rapid intensification of Hurricane Katrina*', PhD thesis. Monash University: Melbourne, Australia.

Nguyen C, Smith R, Zhu H, Ulrich W. 2002. A minimal axisymmetric hurricane model. *Q. J. R. Meteorol. Soc.* **128**: 2641–2661.

Nguyen S, Smith R, Montgomery M. 2008. Tropical-cyclone intensification and predictability in three dimensions. *Q. J. R. Meteorol. Soc.* **134**: 563–582.

Ooyama K. 1969. Numerical simulation of the life cycle of tropical cyclones. *J. Atmos. Sci.* **26**: 3–40.

Puri K, Dietachmayer G, Mills G, Davidson N, Bowen R, Logan L. 1998. The new BMRC Limited Area Prediction System, LAPS. *Aust. Meteorol. Mag.* **47**: 203–233.

Rayleigh L. 1880. On the stability, or instability, of certain fluid motion. *Proc. London Math. Soc.* **11**: 57–70.

Rogers R, Chen S, Tenerelli J, Willoughby H. 2003. A numerical study of the impact of vertical shear on the distribution of rainfall in Hurricane *Bonnie* (1998). *Mon. Weather Rev.* **131**: 1577–1599.

Rozoff C, Schubert W, Brian D, Kossin J. 2006. Rapid filamentation zones in intense tropical cyclones. *J. Atmos. Sci.* **63**: 325–340.

Schecter D, Montgomery M. 2007. Waves in a cloudy vortex. *J. Atmos. Sci.* **64**: 314–337.

Schubert W, Montgomery M, Taft R, Guinn T, Fulton S, Kossin J, Edwards J. 1999. Polygonal eyewalls, asymmetric eye contraction, and potential vorticity mixing in hurricanes. *J. Atmos. Sci.* **56**: 1197–1223.

Shapiro L, Willoughby H. 1982. The response of balanced hurricanes to local sources of heat and momentum. *J. Atmos. Sci.* **39**: 378–394.

Smith R, Montgomery M, Nguyen V. 2009. Tropical cyclone spin-up revisited. *Q. J. R. Meteorol. Soc.* **135**: 1321–1335.

Terwey W, Montgomery M. 2008. Secondary eyewall formation in two idealized, full-physics modeled hurricanes. *J. Geophys. Res.* **113**: D12,112.

Tory K, Montgomery M, Davidson N. 2006. Prediction and diagnosis of tropical cyclone formation in an NWP System. Part I: The critical role of vortex enhancement in deep convection. *J. Atmos. Sci.* **63**: 3077–3090.

Ulrich W, Smith R. 1991. A numerical study of tropical cyclone motion using a barotropic model. Part II. Spatially-varying large-scale flows. *Q. J. R. Meteorol. Soc.* **117**: 107–124.

Wang Y. 2008. Rapid filamentation zone in a numerically simulated tropical cyclone. *J. Atmos. Sci.* **65**: 1158–1181.

Weber H, Smith R. 1993. The stability of barotropic vortices: Implications for tropical cyclone motion. *Geophys. Astrophys. Fluid Dyn.* **70**: 1–30.

Willoughby H. 1990. Temporal changes of the primary circulation in tropical cyclones. *J. Atmos. Sci.* **47**: 242–264.

Willoughby H, Clos J, Shorebah M. 1982. Concentric eye walls, secondary wind maxima, and the evolution of the hurricane vortex. *J. Atmos. Sci.* **39**: 395–411.

Wimmers A, Velden C. 2007. 'MIMIC': A new approach to visualizing satellite microwave imagery of tropical cyclones. *Bull. Am. Meteorol. Soc.* **88**: 1187–1196.

Wissmeier U, Smith R. 2011. Tropical-cyclone convection: The effects of ambient vertical vorticity. *Q. J. R. Meteorol. Soc.* In Press.

Zehr RM. 2006. Analysis of high resolution infrared images of hurricanes from polar satellites as a proxy for GOES-R 4th GOES-R Users' Conference. 1–3 May, Broomfield, CO..

Zhu H, Smith R, Ulrich W. 2001. A minimal three-dimensional tropical cyclone model. *J. Atmos. Sci.* **58**: 1924–1944.

